Journal of Materials Chemistry A

Accepted Manuscript

ROYAL SOCIETY OF CHEMISTRY

www.rsc.org/materialsA

The table of contents entry

Graphene-templated formation of 3D tin-based foams for lithium ion storage application with long lifespan

*Bin Luo, Tengfei Qiu, Long Hao, Bin Wang, Meihua Jin, Xianglong Li, and Linjie Zhi**

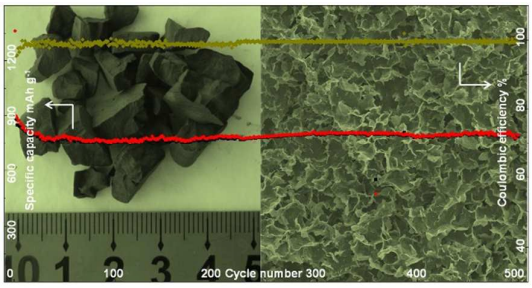

3D graphene-templated tin-based foams with tuneable pore structure and uniform carbon coating have been successfully developed, achieving superior cycling stability and rate capability for lithium ion storage.

Journal Name

COMMUNICATION

Graphene-templated formation of 3D tin-based foams for lithium ion storage application with long lifespan

Received 00th January 20xx,
Accepted 00th January 20xx

DOI: 10.1039/x0xx00000x

www.rsc.org/

*Bin Luo, Tengfei Qiu, Long Hao, Bin Wang, Meihua Jin, Xianglong Li, and Linjie Zhi**

3D tin-based foams with tailorable pore structure are developed through a graphene-templated freeze-drying approach. Pore structure effects on the electrochemical properties of the G/SnO_2@C composite foam are investigated. Further carbon coating endows the foam-like nanocomposite with superior cycling stability and rate capability.

Lithium ion batteries (LIBs) have attracted great attention in the scientific and industrial fields due to their high electromotive force and high energy density.[1, 2] Tremendous efforts have been made to develop new types of electrode materials or structures.[3-6] In the last few years, graphene has attracted great attention for LIBs owing to its high surface area, excellent electrical conductivity, and good compatibility with other electrochemically active components.[7-9] Particularly, three dimensional (3D) porous graphene based inorganic nanocomposites provide promising alternative to traditional electrode materials due to their unique structure-determined properties.[10-23] In most cases, graphene can not only serve as a 2D carbonaceous platform for the deposition of inorganic components, but also be utilized as the building block to construct porous nanostructured networks benefiting for the high rate transportation of lithium ions and charge carriers.

Pore characteristics, such as surface area, pore structure and pore size distributions of electrode materials have been demonstrated to have great influence on the electrochemical performance of LIBs.[3, 24] Owing to its flexible nature, graphene nanosheets can be shrinked or spreaded depending on the synthesis conditions, and thus, leading to formation of 3D graphene based macroforms with different pore structure.[25-28] In the case of graphene based composites, pore structure, one of the important morphology features, also highly depends on the assembly strategy of the composites.[7, 17, 29] For instance, freeze-drying assisted methods have been reported to construct foam-like 3D graphene based nanocomposites[10, 14], during which the interlinked graphene nanosheets can be well kept flat without shrinkage, and thus leading to the porous structure with abundant macropores. The wrinkling degree of graphene sheets and the resulted pore structures of the hybrid structures are expected to have a significant impact on their electrochemical properties, which is rarely reported and of great importance to deeply understand the mechanism of the lithium storage process occurring in such graphene based system.

Herein, we report a facile approach to prepare 3D graphene templated tin-based foams with tailorable pore structure through a freeze-drying assisted method. By investigating pore structure effects on the electrochemical properties of G/SnO_2 based nanocomposites, we find that the foam like G/SnO_2 composite with spreaded graphene structure present more serious capacity decay than the oven dried rigid sample due to its more exposed surfaces of metal oxide. Further carbon coating layer endows the foam-like G/SnO_2@C with superior cycling stability and rate capability. More interestingly, 3D SnO_2 foam (F-SnO_2) and SnS_2 foam (F-SnS_2) with a well-inherited porous structure from F-G/SnO_2 can be obtained after removing the graphene network template by calcination in air and sulfuration in hydrogen sulfide subsequently, opening up new opportunities in synthesizing graphene based nanostructures for practical applications.

The overall synthetic procedure of the graphene/tin oxide foams with different pore structure is illustrated in **Fig. 1**. G/SnO_2 hydrogel with uniform distributed tin oxide on graphene surfaces was firstly synthesized through an *in-situ* hydrolysis method using graphene oxide and stannous chloride as precursors. Then, two different drying processes were applied to remove the water from the hydrogel as shown in Fig. 1a. In one case, the oven drying method (herein vacuum oven drying at 100℃) was adopt, resulting in a very rigid G/SnO_2 composite, named R-G/SnO_2, with an apparent volume

Key Laboratory of Nanosystem and Hierarchical Fabrication, National Center for Nanoscience and Technology, Beiyitiao No. 11, Zhongguancun, Beijing, 100190, P. R. China. E-mail: zhilj@nanoctr.cn; Fax: +86 10 82545578; Tel: +8610 82545578.

Electronic Supplementary Information (ESI) available: Experimental details for the synthesis of graphene templated tin-based foams, and Fig. S1–S8. See DOI: 10.1039/x0xx00000x

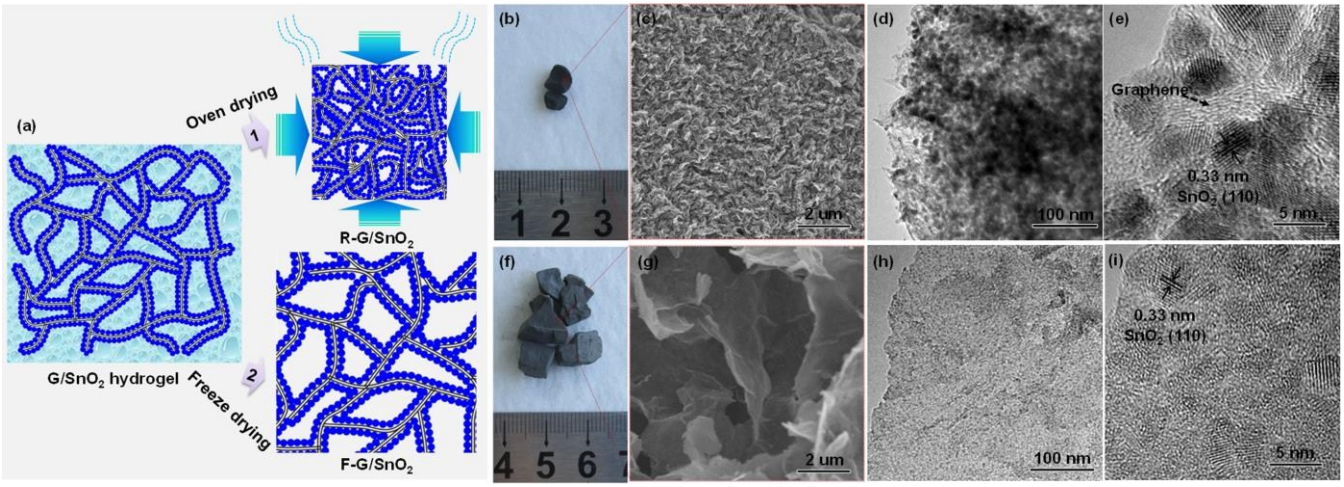

Fig. 1 a) Schematic illustration of the preparation of G/SnO_2 nanocomposites with different pore structures using oven dry and freeze dry approaches, respectively. Photographs, SEM, TEM and HRTEM images of the b-d) R-G/SnO_2 and f-h) F-G/SnO_2 composites.

shrinkage of about one-tenth the volume of the hydrogel. In another, freeze drying method was applied to form a highly porous foam-like G/SnO_2 (F-G/SnO_2) composite with similar morphology of the parent hydrogel without visible shrinkage. Photographs of these two composites with the same weight (200 mg) shown in Fig. 1b and 1f give a visual comparison of the volume difference. The apparent density, the mass per unit volume of material including voids inherent in the material, is calculated according to the mass and the physical dimensions of each sample (see supporting information). As a consequence, F-G/SnO_2 presents a much lower apparent density (~0.32 g cm^{-3}) than the R-G/SnO_2 sample (~3.94 g cm^{-3}). It is reasonable to conclude that the apparent density of the foam-like G/SnO_2 composites can be tailored by rational combination of these two drying processes.

Scanning electron microscopy (SEM) and Transmission electron microscopy (TEM) measurements were further carried out to investigate the structure difference at the micro/nanoscale. From their SEM and TEM images at relatively low magnification, it is clear to see that the R-G/SnO_2 is seriously shrinked into a dense structure after the oven-drying process (Fig. 1c, d), while well-spreaded graphene-like nanosheets can be observed in F-G/SnO_2 after the freeze drying (Fig. 1g, h). The high resolution TEM (HRTEM) images (Fig. 1e, i) show clear lattice fringes of SnO_2 nanoparticles in both cases with a d-spacing of 0.33 nm, which is ascribed to the (110) plane of rutile SnO_2 (JCPDS No. 41-1445). It is also clear to see that tin oxide nanoparticles in R-G/SnO_2 shows higher crystallinity than those in F-G/SnO_2 owing to the thermal treatment during the oven drying process, which is consistent with the X-ray diffraction (XRD) results (Fig. S1). Few-layered graphene sheets that are closely contacted with the nearby SnO_2 nanoparticles can be observed from Fig. 1e for R-G/SnO_2. However, for F-G/SnO_2, it is difficult to see any lattice fringes from graphene nanosheets because the spreaded graphene sheets covered by SnO_2 nanoparticles are prone to lie flat on the copper grid during TEM observation. More detailed information about the porous structure is obtained by nitrogen adsorption measurements. F-G/SnO_2 exhibits a Type I isotherm during which obvious micropore filling occurs at low relative pressure and the adsorption process quickly reaches a well-defined plateau (Fig. S2a), while R-G/SnO_2 presents hybrid features combining Type I isotherms at low relative pressure and IV isotherms with a H3 hysteresis loop at high relative pressure of 0.5-1. An obvious hysteresis loop indicates the existence of a large amount of mesopores of non-rigid slit-shaped pores. Pore size distribution (PSD) curves (Fig. S2b) give more detailed information on their pore structures. Two distinct peaks at ~0.6 nm and ~1.2 nm were observed in the micropore range for F-G/SnO_2, indicating that the freeze dried sample is nearly free of mesopores. These micropores might be derived from the surface defects of graphene nanosheets together with the densely distributed SnO_2 nanoparticles. Except for a silmilar micropores distribution with F-G/SnO_2, large amount of mesopores with a broad range in size (~5-50 nm) were also observed for R-G/SnO_2 sample (Fig. S2b). The specific surface area of R-G/SnO_2 measured by the BET method is 186.5 m^2 g^{-1}, which is larger than that of F-G/SnO_2 (161.3 m^2 g^{-1}). The great difference in the morphology and microstructure of R-G/SnO_2 and F-G/SnO_2 obtained from different drying techniques can be explained by a similar mechanism for the graphene-based network drying process.[25] In the oven drying case, the strong interaction between water and G/SnO_2 nanosheets would results in the shrinkage of the 3D network when water evaporate gradually, resulting a large amount of mesopores with a broad range in size. In the freeze drying case, the 3D foam like morphology can be remained due to the phase separation and weak interaction between the frozen ice crystals and G/SnO_2 based network.

As the electrode materials, the direct exposed metal oxide nanoparticles on graphene surfaces of G/SnO_2 are prone to disintegrate or break down due to the volume expansion and aggregation of these active nanoparticles.[12, 30] In view of this, a thin layer of carbon is coated onto the surface of F-G/SnO_2 by glucose hydrothermal carbonization method as illustrated in **Fig.**

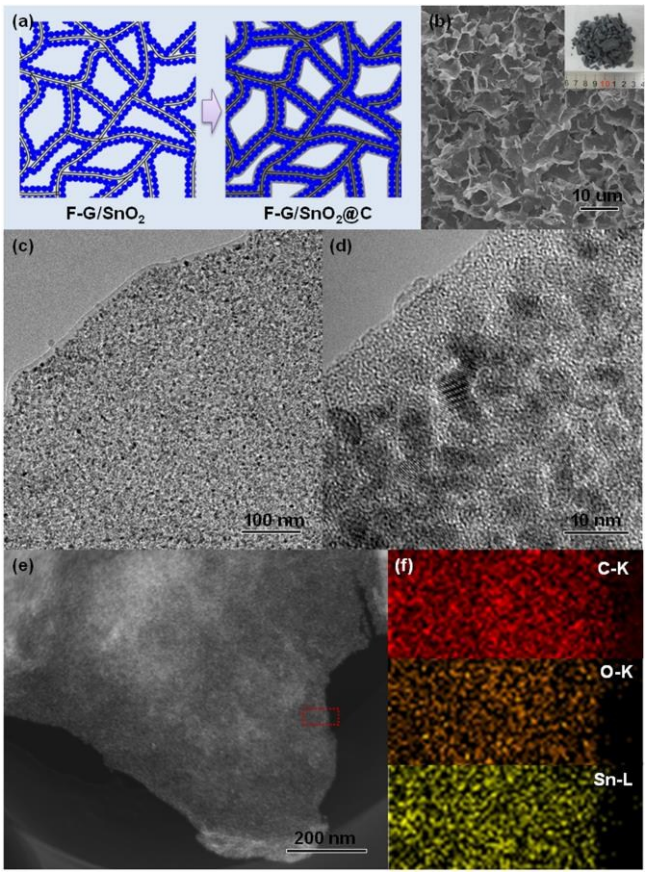

Fig. 2 a) Schematic illustration of the hydrothermal synthesis of carbon coated graphene/SnO_2 foam (F-G/SnO_2@C) using F-G/SnO_2 as precusor. b) Photograph of F-G/SnO_2@C shows its similar foam-like apparence with F-G/SnO_2 without carbon coating. c, d) TEM, e) STEM images, and f) carbon, oxygen, and tin element mapping images of the G/SnO_2@C foam, demonstrating the morphology and microstructure of the 3D porous foam composed of 2D graphene based composite nanosheets with uniformly distributed tin oxide nanoparticles and a thin layer of carbon coating on both surfaces.

2a.[16] SEM image (Fig. 2b) and the inserted Photograph show F-G/SnO_2@C exhibits a similar highly porous structure with the uncoated F-G/SnO_2. Detailed component and microstructure of the F-G/SnO_2@C can be observed by TEM and STEM characterizations. As shown in Fig. 2c-e, the pre-loaded tin oxide nanoparticles with an average diameter of 5 nm on the graphene surfaces are evenly covered by an amorphous carbon layer with the thickness of approximately 5 nm. The homogeneous distribution of SnO_2 nanoparticles in the F-G/SnO_2@C nanocomposites can be confirmed by the elemental mapping of the composite for C, Sn, and O (Fig. 2f). The broad diffraction peaks in XRD patterns (Fig. S1) for the F-G/SnO_2 nanocomposites before and after carbon coating indicate the small crystal size of tetragonal rutile SnO_2 phase in both of them, which are consistent with the TEM results. Furthermore, thermogravimetric analysis (TGA) was carried out to determine the chemical composition of the F-G/SnO_2 composite before and after carbon coating (Fig. S3). The results show that the SnO_2 contents in F-G/SnO_2 and F-G/SnO_2@C composites are ~92.0 wt % and ~75.8 wt % respectively. The F-G/SnO_2@C present a slightly higher apparent density (~0.39 g cm^{-3}) than F-G/SnO_2 after carbon coating. For comparison, the above R-G/SnO_2 composite was coated with a thin layer of carbon using the same method and its structural information are provided in the supporting file (Fig. S4). Similar porous structure based on distinctly curved graphene network substrate can be observed for both R-G/SnO_2 and R-G/SnO_2@C composites.

The graphene/tin oxide based nanocomposites in this work are attractive as anode materials for LIBs. Here we investigated the electrochemical performance of the as-prepared composites by galvanostatic charge/discharge cycling in a coin cell using lithium metal as the counter electrode. In order to get better comparability, the same areal mass-loading of active material (~1.0 mg cm^{-2}) was applied to each sample. **Fig. 3a** shows the specific capacity as a function of cycle number for the R-G/SnO_2 and F-G/SnO_2 composites before and after carbon coating at a constant current density of 100 mA g^{-1}. Notably, the F-G/SnO_2@C composite delivers a reversible capacity of 889 mAh g^{-1} which can be maintained up to 820 mAh g^{-1} after 100 cycles at a current density of 100 mA g^{-1}. In contrast, the F-G/SnO_2 without carbon coating exhibits fast capacity decay after 30 cycles, which is in agree with the results reported recently.[30] Interestingly, in spite of the nearly equal weight content of SnO_2 for R-G/SnO_2 and F-G/SnO_2 composites, the specific capacity of the former exhibits a much better cycling performance with a slower decreasing capacity than F-G/SnO_2 (Fig. 3a). This can be ascribed to the much more exposed surfaces of metal oxide in F-G/SnO_2 than R-G/SnO_2 due to the large amount of macropores existing in the former, while the seriously shrinked graphene network in R-G/SnO_2 can preserve the cycling stability to some extent. An improved cycling performance has also been obtained for R-G/SnO_2@C after carbon coating, while the reversible capacity value (848 mAh g^{-1}) is much lower than the foam-like sample (959 mAh g^{-1}). What's more, the rate performance of F-G/SnO_2@C is also superior to the R-G/SnO_2@C electrode, for the former a high rate capacity up to 480 mAh g^{-1} at 3200 mA g^{-1} could be achieved as shown in Fig. 3b. This might be also attributed to the relative compact structure of R-G/SnO_2@C which is not in favor of the lithium ion diffusion process. Electrochemical impedance spectroscopy (EIS) measurements were further carried out to compare the reaction kinetics of the F-G/SnO_2@C and R-G/SnO_2@C electrodes after 100 cycles (Fig. S5). The Nyquist plots of the composites are mainly composed of one high-frequency depressed semicircle and a low-frequency sloping line, which are associated with the interfacial impedances and Warburg-type diffusion impedance, respectively. The diameter of the semicircle for F-G/SnO_2@C in the high frequency region is smaller than that of R-G/SnO_2@C electrode, indicating that F-G/SnO_2@C possess lower contact and charge-transfer resistances. Moreover, the steeper sloping line of F-G/SnO_2@C anode at low frequencies than that of R-G/SnO_2@C demonstrates the diffusion transport of Li ions in F-G/SnO_2@C is much easier than that in R-G/SnO_2@C. These

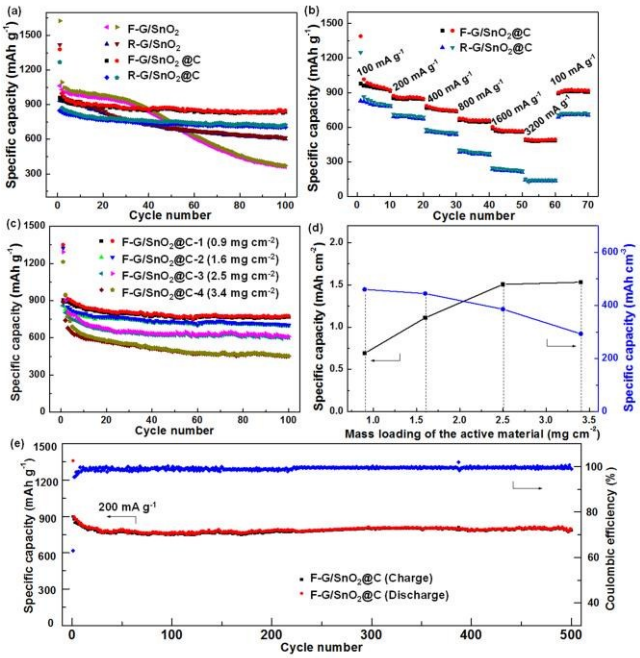

Fig. 3 a) Cycle performance of R-G/SnO_2, F-G/SnO_2, R-G/SnO_2@C and F-G/SnO_2@C electrodes at a rate of 100 mA g^{-1} and b) the rate performance of R-G/SnO_2@C and F-G/SnO_2@C electrodes at various current densities. c) Gravimetric capacities, and d) areal and volumetric capacities of F-G/SnO_2@C anodes with various mass loading of active material (~0.9, 1.6, 2.5, and 3.4 mg cm^{-2}) at a current sensity of 200 mA g^{-1}, respectively. e) Cycle performance of F-G/SnO_2@C electrode at a rate of 200 mA g^{-1}.

results validates that F-G/SnO_2@C anode has better rate capability than R-G/SnO_2@C for Li-ion storage.

From a practical point of view, the areal capacity and volumetric capacity are another two critically important technical indicators for commercialization of anodes. The areal capacity of the F-G/SnO_2@C can be potentially increased by increasing the areal mass loading of active materials. Fig. 3c displays the gravimetric capacities of the F-G/SnO_2@C electrodes with various active material mass loading of ~0.9, 1.6, 2.5, and 3.4 mg cm^{-2} at a current sensity of 200 mA g^{-1}, the thickness of which were measured to be ~15, 25, 38 and 56 μm, respectively (Fig. S6, Table S1). These electrodes present a significant increase in areal capacity with the increasing of the areal mass loading of active material as shown in Figrue 5b. The slightly decreased gravimetric capacity can be ascribed to the long Li-ion diffusion path caused by the increase of the electrode thickness. The volumetric capacity, which mainly depended on the tap density of active materials, can be enhanced by removing the macropores inside the foam via further grinding and pressing method.[12] The average tap density of the above four F-G/SnO_2@C electrodes is in the range of 0.60~0.65 g cm^{-3} (see supporting information Table S1), which is much higher than the apparent density of F-G/SnO_2@C (~0.39 g cm^{-3}). As a result, the volumetric capacities of the F-G/SnO_2@C anodes are significantly enhanced by further grinding and pressing process, although the volumetric capacity value gradually decreases with the increase of the electrode thickness (Fig. 3d). We note that there is still large room for increasing the capacity values of the F-G/SnO_2@C, for example, by optimizing the carbon coating thickness and the weight ratio of active component to conductive additive and polymer binder. Remarkably, the cycling performance at a current density of 200 mA g^{-1} (Fig. 3e) indicates that the F-G/SnO_2@C still delivers a high reversible specfic capacity of 785 mAh g^{-1} even with a long life span of 500 cycles, which is superior to the literature reported graphene based SnO_2 nanocomposites.[23, 31-35]

To further understand the outstanding electrochemical performance of F-G/SnO_2@C composite, SEM and TEM measurement (Fig. S7) has been performed to observe the morphological change of the electrode after 100 cycles at a rate of 100 mA g^{-1}. It is clearly seen that the F-G/SnO_2@C anode still retains its original appearance after repeated cycles. Notably, all SnO_2 NPs are well confined in the 2D carbon matrix, further demonstrating that the unique structure of the composite could effectively alleviate the pulverization and prevent the particle aggregation. The excellent electrochemical performance of the F-G/SnO_2@C composite could be attributed to the following reasons: 1) The F-G/SnO_2@C composite with high porosity is more favorable for electrolyte accessibility and rapid lithium-ion diffusion than the R-G/SnO_2@C with relatively compact structure. 2) The carbon coating layer not only anchor the SnO_2 nanoparticles on the surface of graphene effectively, but also improve the conductivity of the electrode. The improved initial columbic efficiency is also mainly attributed to the conducting carbon layer (Fig. S8), which leads to the formation of uniform thin SEI films on the surface of the composites to reduce the capacity loss at the first discharge/charge cycle.[30, 36]

As n-type semiconductors with wide band gaps, both tin oxide and tin sulfide nanostructures with high porosity and specific surface area are desired for many applications such as sensors, solar cells, and catalysis.[37, 38] It should be noted that the G/SnO_2 foam can be easily transformed to porous tin oxide foam and tin sulfide foam by simply calcination in air and sulfuration in H_2S/Ar mixture gas subsquently. As illustrated in **Fig. 4a, b**, the apparent color change from black to white and golden yellow can be observed after removal of graphene and the consequent sulfuration. SEM images (Fig. 4c and 4e) show that both the SnO_2 and SnS_2 foams perfectly inherit the geometric morphology of the G/SnO_2 parent foam. High resolution SEM image (Fig. 4d) shows that the SnO_2 foam is composed of interlinked tin oxide nanoparticles, presenting the uniform also continuous coating of tin oxide nanoparticles on graphene surfaces. As to the SnS_2 foam, tin nanoparticles are *in situ* transformed into tin sulfide nanoplates after sulfuration (Fig. 4f), forming a 3D highly porous metal sulfide nanostructure. XRD result (Fig. S9) further confirms the 2T-type layered structure (JCPDS No. 23-0677) of the obtained SnS_2 nanoplates. It is reasonable to consider that this graphene-templated strategy is also applicable to prepare other kinds of 3D metal oxide or sulfide nanostructures, which definitely extend their applications in other areas.

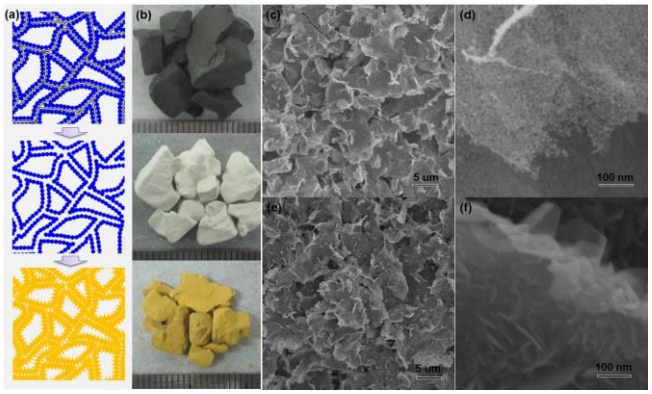

Fig. 4 a) Transformation of F-G/SnO_2 to SnO_2 foam (F-SnO_2) and SnS_2 foam (F-SnS_2) by calcination in air and sulfuration in H_2S/Ar mixture gas subsquently. b) Photographs of F-G/SnO_2 (top), F-SnO_2 (middle), and F-SnS_2 (bottom) show the color change of the foams after calcination and sulfuration. SEM images of c, d) F-SnO_2 and e, f) F-SnS_2 showing their inherited 3D porous structure from the G/SnO_2 foam without damage after calcination and and sulfuration at a high temperature.

Conclusions

In summary, 3D tin-based nanostructures with adjustable pore structures have been developed through a freeze-drying assisted approach, during which the interlinked graphene network template serves as not only a substrate for precursors loading but also a platform for the chemical conversion reactions. The influences of pore structures and carbon coating on the electrochemical properties of G/SnO_2 composites are investigated. When evaluated as a anode material for LIBs, the oven-dried G/SnO_2 composite exhibits better cycling stability than the freeze-drying derived G/SnO_2 sample, while a further carbon coating endows F-G/SnO_2@C with a superior cycling stability and rate capability. Furthermore, with the foam-like G/SnO_2 composite as starting materials, the successful synthesis of tin oxide and tin sulfide foams after graphene removal by calcination and sulfuration subsquently further highlight the versatile nature of the graphene based inorganic nanocomposites that definitely extends their applications.

Acknowledgements

Financial support from the Ministry of Science and Technology of China (No. 2012CB933403), the National Natural Science Foundation of China (Grant No. 21173057, 51425302), the Beijing Municipal Science and Technology Commission (Z121100006812003), and the Chinese Academy of Sciences is acknowledged.

Notes and references

1 S. Chu and A. Majumdar, *Nature*, 2012, **488**, 294.
2 J. M. Tarascon and M. Armand, *Nature*, 2001, **414**, 359.
3 M. G. Kim and J. Cho, *Adv. Funct. Mater.*, 2009, **19**, 1497.
4 A. L. M. Reddy, S. R. Gowda, M. M. Shaijumon and P. M. Ajayan, *Adv. Mater.*, 2012, **24**, 5045.
5 M. V. Reddy, G. V. S. Rao and B. V. R. Chowdari, *Chem. Rev.*, 2013, **113**, 5364.
6 Q. F. Zhang, E. Uchaker, S. L. Candelaria and G. Z. Cao, *Chem. Soc. Rev.*, 2013, **42**, 3127.
7 S. Han, D. Wu, S. Li, F. Zhang and X. Feng, *Small*, 2013, **9**, 1173.
8 B. Luo, S. Liu and L. Zhi, *Small*, 2012, **8**, 630.
9 G. X. Wang, X. P. Shen, J. Yao and J. Park, *Carbon*, 2009, **47**, 2049.
10 Y. Gong, S. Yang, Z. Liu, L. Ma, R. Vajtai and P. M. Ajayan, *Adv. Mater.*, 2013, **25**, 3979.
11 B. Luo, B. Wang, M. Liang, J. Ning, X. Li and L. Zhi, *Adv. Mater.*, 2012, **24**, 1405.
12 W. Wei, S. B. Yang, H. X. Zhou, I. Lieberwirth, X. L. Feng and K. Mullen, *Adv. Mater.*, 2013, **25**, 2909.
13 S. B. Yang, X. L. Feng, S. Ivanovici and K. Mullen, *Angew. Chem. Int. Ed.*, 2010, **49**, 8408.
14 J. Luo, J. Liu, Z. Zeng, C. F. Ng, L. Ma, H. Zhang, J. Lin, Z. Shen and H. J. Fan, *Nano Lett.*, 2013, **12**, 6163.
15 S. M. Paek, E. Yoo and I. Honma, *Nano Lett.*, 2009, **9**, 72.
16 B. Luo, B. Wang, X. Li, Y. Jia, M. Liang and L. Zhi, *Adv. Mater.*, 2012, **24**, 3538.
17 S. Bai and X. Shen, *Rsc Adv.*, 2012, **2**, 64.
18 Z. S. Wu, W. C. Ren, L. Wen, L. B. Gao, J. P. Zhao, Z. P. Chen, G. M. Zhou, F. Li and H. M. Cheng, *ACS Nano*, 2010, **4**, 3187.
19 B. Luo, Y. Fang, B. Wang, J. Zhou, H. Song and L. Zhi, *Energ Environ. Sci.*, 2012, **5**, 5226.
20 B. Luo and L. J. Zhi, *Energ Environ. Sci.*, 2015, **8**, 456.
21 P. C. Lian, X. F. Zhu, S. Z. Liang, Z. Li, W. S. Yang and H. H. Wang, *Electrochim. Acta*, 2011, **56**, 4532.
22 G. X. Wang, B. Wang, X. L. Wang, J. Park, S. X. Dou, H. Ahn and K. Kim, *J. Mater. Chem.*, 2009, **19**, 8378.
23 S. Yang, W. Yue, J. Zhu, Y. Ren and X. Yang, *Adv. Funct. Mater.*, 2013, **23**, 3570.
24 A. S. Arico, P. Bruce, B. Scrosati, J. M. Tarascon and W. Van Schalkwijk, *Nat. Mater.*, 2005, **4**, 366.
25 Y. Tao, X. Y. Xie, W. Lv, D. M. Tang, D. B. Kong, Z. H. Huang, H. Nishihara, T. Ishii, B. H. Li, D. Golberg, F. Y. Kang, T. Kyotani and Q. H. Yang, *Sci. Rep.*, 2013, **3**, 2975.
26 Y. X. Xu, K. X. Sheng, C. Li and G. Q. Shi, *ACS Nano*, 2010, **4**, 4324.
27 F. Liu and T. S. Seo, *Adv. Funct. Mater.*, 2010, **20**, 1930-1936.
28 Y. W. Zhu, S. Murali, W. W. Cai, X. S. Li, J. W. Suk, J. R. Potts and R. S. Ruoff, *Adv. Mater.*, 2010, **22**, 3906.
29 W. W. Zhou, J. X. Zhu, C. W. Cheng, J. P. Liu, H. P. Yang, C. X. Cong, C. Guan, X. T. Jia, H. J. Fan, Q. Y. Yan, C. M. Li and T. Yu, *Energ Environ. Sci.*, 2011, **4**, 4954.
30 Y. Z. Su, S. Li, D. Q. Wu, F. Zhang, H. W. Liang, P. F. Gao, C. Cheng and X. L. Feng, *ACS Nano*, 2012, **6**, 8349.
31 X. Y. Wang, X. F. Zhou, K. Yao, J. G. Zhang and Z. P. Liu, *Carbon*, 2011, **49**, 133.
32 S. J. Ding, D. Y. Luan, F. Y. C. Boey, J. S. Chen and X. W. Lou, *Chem. Commun.*, 2011, **47**, 7155.
33 J. Yao, X. P. Shen, B. Wang, H. K. Liu and G. X. Wang, *Electrochem. Commun.*, 2009, **11**, 1849.
34 L. S. Zhang, L. Y. Jiang, H. J. Yan, W. D. Wang, W. Wang, W. G. Song, Y. G. Guo and L. J. Wan, *J. Mater. Chem.*, 2010, **20**, 5462.
35 S. Ding, D. Luan, F. Y. C. Boey, J. S. Chen and X. W. Lou, *Chem. Commun.*, 2011, **47**, 7155.
36 X. W. Lou, J. S. Chen, P. Chen and L. A. Archer, *Chem. Mater.*, 2009, **21**, 2868.
37 M. Batzill and U. Diebold, *Prog. Surf. Sci.*, 2005, **79**, 47.

38 Y. F. Sun, H. Cheng, S. Gao, Z. H. Sun, Q. H. Liu, Q. Liu, F. C. Lei, T. Yao, J. F. He, S. Q. Wei and Y. Xie, *Angew. Chem. Int. Ed.*, 2012, **51**, 8727.